Asian Journal of Chemistry; Vol. 37, No. 8 (2025), 2072-2080

ASIAN JOURNAL OF CHEMISTRY

https://doi.org/10.14233/ajchem.2025.34205

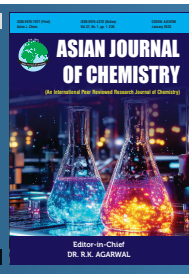

Visible-Light-Activated Graphitic Carbon Nitride/CdS Heterostructure for Superior Photocatalytic Removal of Amoxicillin

PANDURANGAN VIJAYALAKSHMI[1,*] and VISNU SASITHRA[2]

[1]Department of Radiology, Saveetha Medical College, Saveetha Institute of Medical and Technical Science, Chennai-602105, India
[2]Department of Orthopaedics, Saveetha Medical College and Hospital, Saveetha Institute of Medical and Technical Sciences, Saveetha University, Chennai-602105, India

*Corresponding author: E-mail: vijidr1203@gmail.com

Received: 6 June 2025; *Accepted*: 28 July 2025; *Published online*: 31 July 2025; AJC-22087

In this study, a S-scheme graphitic carbon nitride/cadmium sulfide (g-C_3N_4/CdS) nanocomposite was synthesized as well as evaluated of its photocatalytic efficiency within degrading amoxicillin (AMX) from aqueous solutions underneath visible-light exposure. The structural as well optical properties of the nanocomposite were characterized using X-ray diffraction (XRD), UV-Vis diffuse reflectance spectroscopy (UV-DRS), scanning electron microscopy (SEM) and electrochemical impedance spectroscopy (EIS). The g-C_3N_4/CdS nanocomposite exhibited a narrow band gap of 1.9 eV and achieved an impressive AMX degradation efficiency of 87.08% (rate constant k = 0.0149 min^{-1}) within 150 min, surpassing the performance of the bare nanocomponents. Reactive species trapping experiments identified photogenerated holes (h^+) as well as superoxide radicals ($O_2^{\bullet-}$) as the dominant species of active in the degradation processes. Moreover, the photocatalyst demonstrated excellent reusability and chemical stability over three successive cycles, underscoring its potential for practical applications in the removal for organic contaminants in water.

Keywords: g-C_3N_4/CdS nanocomposite, Photocatalysis, Visible light degradation, Organic pollutant removal.

INTRODUCTION

The widespread utilized of antibiotics of both human healthcare as well animal husbandry was led to their frequent detection in the environment. Due to their poor absorption by organisms, a significant portion of administered antibiotics and their pharmacologically active metabolites are excreted unchanged through urine and feces [1,2]. These residues enter water bodies and soils, where they persist due to their low biodegradability under aerobic conditions.

Amoxicillin (AMX), a β-lactam antibiotic, is among the most commonly detected pharmaceutical pollutants in surface waters, wastewater and sediments. The persistent presence of antibiotics like AMX poses serious environmental and health concerns, particularly the development of antibiotic-resistant bacteria [3]. Traditional biological wastewater treatment processes often fail to fully eliminate antibiotics, primarily due to the antimicrobial nature of these compounds, which disrupt microbial activity [4-6]. Hence, there is an urgent need for the alternative, cost-effective and environmentally sustainable methods for the efficient removal of antibiotics from aquatic systems [7,8].

Advanced oxidation processes (AOPs), including anodic oxidation, ozonation, electrochemical degradation, adsorption and photocatalysis, has been widely explored of the degradation for such pollutants [8]. Among these, photocatalysis has garnered significant attention due to its capability to mineralize a wide range for organic pollutants under light irradiation. However, conventional photocatalysts like titanium dioxide (TiO_2) are limited by their wide band gap (~3.2 eV), it restricts their photoactivity in the ultraviolet (UV) region, accounting of only about 4% of the solar spectrum [9,10]. Graphitic carbon nitride (g-C_3N_4) emerged as a promising visible-light-driven photocatalyst, within a moderate band gap (~2.7 eV) that allows absorption of a broader range of the solar spectrum (~43%). Its advantages include a 2D layered structure, good thermal also chemical stability, as well as favourable electronic properties [11]. Nevertheless, pure g-C_3N_4 suffers from intrinsic limitations

like low specific surface area, high recombination rate for photogenerated charge carriers, as well as limited visible-light utilization efficiency [12]. To address these drawbacks, several modifi-cation strategies have been developed, like elemental doping, coupling within other semiconductors to form heterojunctions and co-catalyst loading (*e.g.* Pt, Pd, Cu, Co_3O_4).

Cadmium sulfide (CdS), with a narrow band gap for ~2.4 eV, is capable in absorbing visible light up to ~520 nm. It has been widely studied as a sensitizer for enhance the visible-light response of photocatalysts [13]. However, CdS is prone to photocorrosion due to oxidation of sulfide (S^{2-}) ions by photogenerated holes and its photocatalytic efficiency is further hindered by rapid charge carrier recombination. Fortunately, the conduction and valence band positions for CdS also *g*-C_3N_4 are well-aligned, making them ideal candidates for constructing heterostructures that can improve charge separation as well as enhance the photocatalytic performance [14,15]. In such composites, the migration for photogenerated holes from the valence band in CdS to *g*-C_3N can suppress photocorrosion and improve stability. Although *g*-C_3N_4/CdS composites have been widely reported, most of them involve conventional type-II heterojunctions rather than direct S-scheme or S-scheme systems, which offer superior redox ability and charge separation efficacy. In this study, a S-scheme *g*-C_3N_4/CdS nanocomposite was successfully synthesized *via* a simple two-step process. The photocatalytic activity for the composite has evaluated for the degradation of amoxicillin underneath visible light irradiation.

EXPERIMENTAL

All chemicals as well reagents were of analytical reagent (A.R.) grade and used without any additional purification. Urea (CH_4N_2O, 99.5% purity), citric acid monohydrate ($C_6H_8O_7{\cdot}H_2O$, 99%), cadmium chloride hemipentahydrate ($CdCl_2{\cdot}2.5H_2O$), thioacetamide (TAA), ammonia solution and ethanol (C_2H_5OH, 98%) were sourced from Merck Ltd., India and used as provided. For the radical scavenging studies, benzoquinone ($C_6H_4O_2$, 98%), ethylenediaminetetraacetic acid (EDTA, $C_{10}H_{16}N_2O_8$, 99%) and isopropanol (C_3H_8O, 98%) were employed. All experiments have conducted utilizing deionized water obtained in a Milli-Q ultrapure water purification system.

Synthesis of CdS/*g*-C_3N_4 binary nanocomposite: Graphitic carbon nitride (*g*-C_3N_4) nanosheets was initially synthesized following a reported method [16,17]. Briefly, a specific quantity of urea was subjected to thermal treatment at 570 ºC for 3 h in an open-air environment, resulting in a yellow powder, which was collected for further processing. Subsequently, 10 mg of the prepared *g*-C_3N_4 nanosheets were dispersed in 20 mL of of $CdCl_2{\cdot}2.5H_2O$ using ultrasonication for 30 min. After dispersion, 0.25 mL of NH_3 solution and 5 mL of TAA (5.5 mg) solution were introduced into the mixture. This suspension was then treated in a water bath at 60 ºC at 3 h. The resulting product has thoroughly washed within deionized water and ethanol multiple times and separated by centrifugation. The obtained material has dried at 60 ºC of 4 h also subsequently annealed in 300 ºC for 2 h under a N_2 atmosphere in a tubular furnace of improve the crystallinity of CdS [18,19] (**Scheme-I**).

Characterization: The synthesized nanoparticles underwent thorough characterization using various analytical techniques. X-ray diffraction (XRD) analysis was carried out utilizing a Bruker Kappa APEX II diffractometer for determine the crystalline structure and phase composition, measuring the 2θ range from 10º to 80º with Cu*K*α radiation. High-resolution

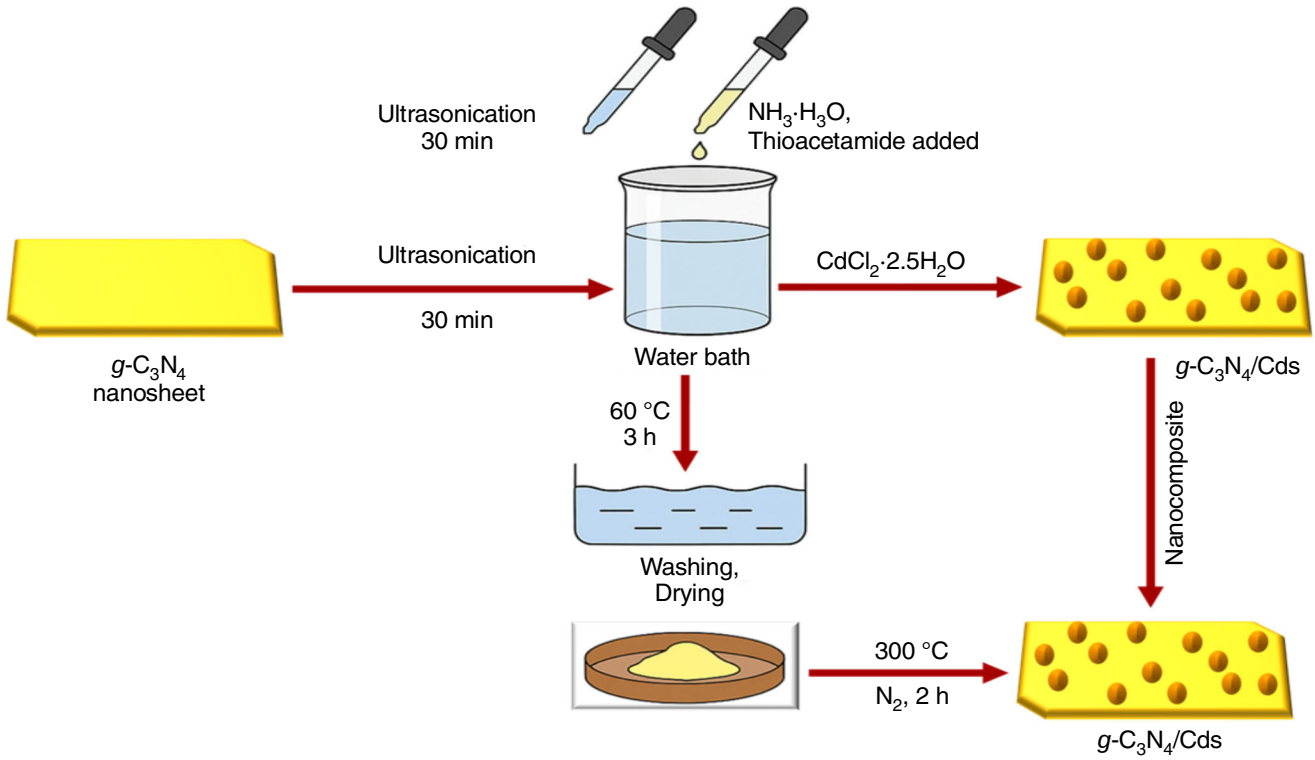

Scheme-I: Schematic representation for the synthesis processes of *g*-C_3N_4/CdS hybrids

scanning electron microscopy (HRSEM, FEI-Quanta FEG 200F) was employed to examine the surface morphology and internal structure of the nanocomposite. The optical behaviour of the composite was evaluated through UV-visible diffuse reflectance spectroscopy (DRS) using a Shimadzu UV-2600 spectrophotometer, covering the wavelength range to 400–800 nm. Electrochemical Impedance Spectroscopy (EIS) measurements, conducted with a Princeton instrument (NJ, USA), were used to analyze the electrical properties and interfacial interactions between the electrode and the electrolyte.

Photocatalysis: The photocatalytic degradation for the organic pollutant amoxicillin (AMX) was carried out with an annular-type Heber photoreactor (model HVAR-MP400). A 300 W Xenon lamp fitted with a 420 nm cutoff filter has utilized as the light source to block wavelengths below 420 nm [20]. For each experiment, 50 mg of synthesized *g*-C_3N_4/CdS nanocomposite has dispersed in 100 mL for an aqueous AMX solution in a concentration for 20 mg/L. Prior to illumination, the suspension was stirred thoroughly in dark for 30 min to achieve the adsorption–desorption equilibrium [21].

Photocatalytic activity was then initiated by placing the mixture in the photoreactor, where the continuous aeration was provided through pumping of ensure uniform dispersion of the catalyst during the reaction process. At 10 min intervals, 5 mL aliquots were withdrawn, centrifuged for 10 min in separate the photocatalyst and the clear supernatant was collected for analysis. The concentration of AMX remaining in the solution was determined using a visible double-beam UV-Vis spectrophotometer by measuring absorbance in its maximum wavelength (λ_{max} = 341 nm) [22].

The degradation efficacy of AMX was calculated by following eqn. 1:

$$\text{Degradation of (AMX) pollution (\%)} = 1 - \frac{C_t}{C_o} \quad (1)$$

where C_o refers to the initial concentration for organic pollutant before the onset of light exposure; C_t indicates the concentration in a given time t during the photocatalytic irradiation. These values represent the pollutant levels prior to and after illumination, accordingly.

RESULTS AND DISCUSSION

Phase structural studies: The powder X-ray diffraction (XRD) analysis was performed to investigate the crystalline structures of *g*-C_3N_4, CdS nanoparticles as well as the *g*-C_3N_4/CdS nanocomposite. The X-ray diffraction (XRD) patterns for the synthesized materials are shown in Fig. 1. In Fig. 1a, the diffraction pattern of bare graphitic carbon nitride (*g*-C_3N_4) displays two prominent peaks at approximately 13.1° and 27.4°, it corresponds of the (100) as well (002) planes, accordingly. The (100) reflection was attributed of the in-plane structural packing for tri-*s*-triazine units, while the (002) reflection is assigned of the interlayer stacking of aromatic conjugated systems, confirming the layered structure for *g*-C_3N_4 [23]. Fig. 1b shows the XRD pattern of cadmium sulfide (CdS), exhibiting multiple sharp peaks at 2θ values corresponding to the (100), (002), (101), (102), (110), (103), (112), (004), (200), (202), (203), (114), (105) planes. These reflections has consistent with the hexagonal wurtzite phase for CdS and matched well with JCPDS card no. 41-1049 [24], indicating its high crystallinity. In Fig. 1c, the *g*-C_3N_4/CdS heterostructure shows characteristic peaks for both *g*-C_3N_4 as well as CdS, confirming the successful formation of the composite. The presence of the (002) peak of *g*-C_3N_4 along with the diffraction peaks of CdS demonstrates that CdS nanoparticles were well-dispersed in the *g*-C_3N_4 nanosheets without altering the crystal structure of either component. The sharpness and intensity of the peaks in the composite also suggest good crystallinity of the hybrid.

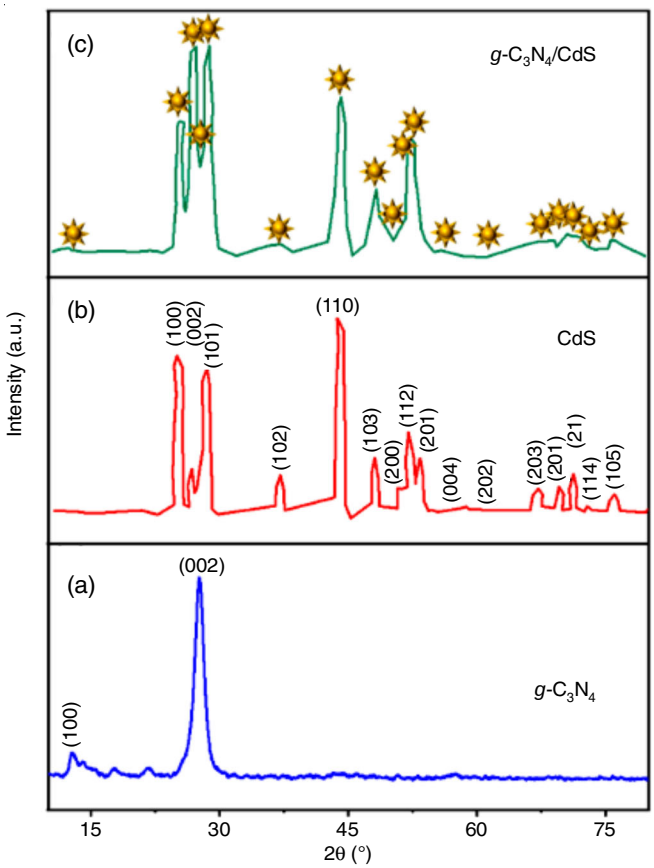

Fig. 1. XRD spectra of (a) *g*-C_3N_4, (b) CdS and (c) *g*-C_3N_4/CdS

Morphological studies: The SEM images of *g*-C_3N_4 possesses a characteristic layered, wrinkled sheet-like structure, reflecting its 2D nature and relatively large surface area (Fig. 2a-b). This flake-like and crumpled texture enhances the distribution of semiconductor nanoparticles and provides an ideal substrate for heterostructure formation [25]. The CdS nanoparticles appear as bright, spherical particles uniformly dispersed across the *g*-C_3N_4 surface, easily identified due to contrast differences arising from their distinct atomic numbers. The close contact between CdS and *g*-C_3N_4 indicates strong interfacial interactions, which are vital for effective charge separation and transfer [26].

The even distribution of CdS in the *g*-C_3N_4 sheets points to the successful formation for a heterojunction, which is crucial for boosting photocatalytic performance under visible light. This morphological structure facilitates efficient charge carrier movement, minimizes recombination for electron-hole pairs,

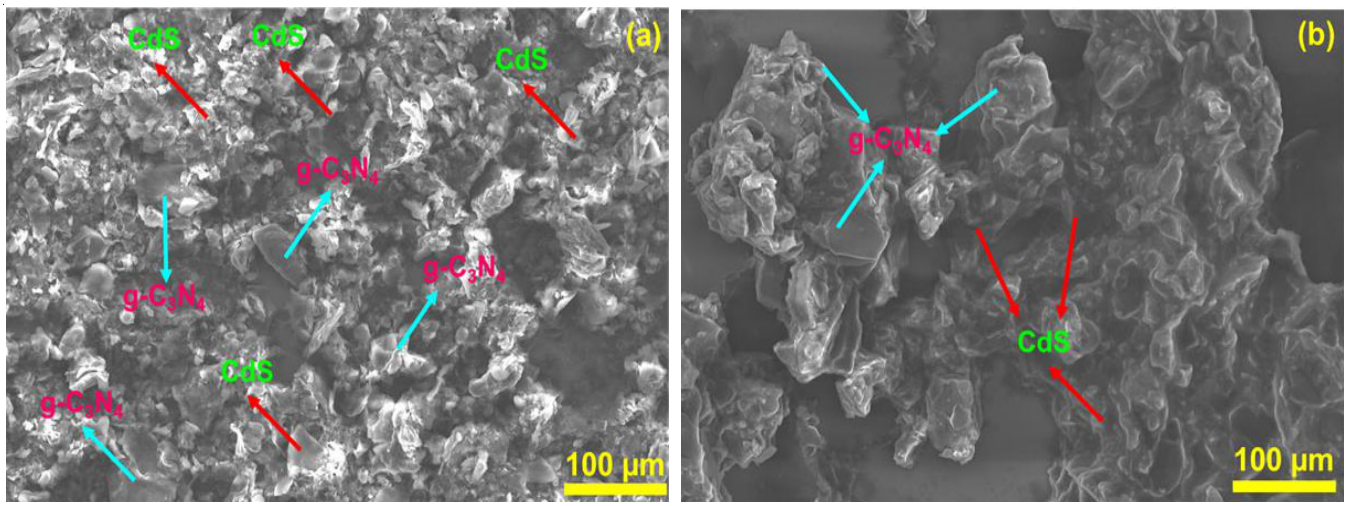

Fig. 2. HRSEM images for synthesized bare nanocomponents as well as nanocomposite g-C_3N_4, CdS and g-C_3N_4/CdS

as well as enhances light in absorption. Overall, SEM analysis confirms the successful incorporation for CdS within the g-C_3N_4 matrix, supporting the intended structural design to improve the photocatalytic efficiency for environmental purification applications [27].

Optical property analysis: The optical properties in the synthesized materials, including g-C_3N_4, CdS, also the g-C_3N_4/CdS nanocomposite, were examined using diffuse reflectance spectroscopy (DRS). The optical behaviour for pure g-C_3N_4 and CdS nanoparticles was examined through UV-Vis diffuse reflectance spectroscopy (DRS) in evaluate their effectiveness underneath visible-light irradiation. The g-C_3N_4 showed a distinct absorption edge around 475 nm (Fig. 3a), indicating its responsiveness to visible light [20]. This absorption arises mainly from π–π* transitions within the sp^2-hybridized conjugated network of its tri-*s*-triazine rings. The band gap energy (E_g) was estimated using a Tauc plot derived from the Kubelka-Munk function, as shown in the inset of Fig. 3a, revealing a band gap for approximately 2.6 eV, slightly lower than the typical value for bulk g-C_3N_4 (2.6 eV). This reduction could be due to improved conjugation or minor structural modifications [21].

CdS nanoparticles, on the other hand, exhibited broad and intense absorption within the visible region, in an absorption edge near 620 nm (Fig. 3b). The corresponding Tauc plot estimated the band gap at around 2.0 eV, aligned with the previously reported values for nanostructured CdS, confirming its effective utilization of visible light [28].

The g-C_3N_4/CdS nanocomposite displayed enhanced optical absorption. Its DRS spectrum showed a significant redshift, within the absorption edge extending to approximately 650 nm (Fig. 3c) [8]. This improved light absorption is attributed to the synergistic coupling between g-C_3N_4 also CdS, which expands the visible-light response range of the composite. The Tauc plot for the nanocomposite revealed a reduced band gap of about 1.9 eV, further confirming its superior capability for visible-light absorption. This narrowed band gap promotes efficient photoexcitation under solar light, making the g-C_3N_4/CdS nanocomposite a strong candidate for photocatalytic applications in environmental cleanup and other solar-driven processes (eqn. 2).

$$F(R) = \frac{(1\times R)^2}{2R} \tag{2}$$

here, R stands for reflectance of measured.

The bandgap energy (E_g) values were estimated utilizing Tauc eqn. 3:

$$(\alpha h\nu)^2 = A(h\nu - E_g) \tag{3}$$

In this context, hν denotes the photon energy, A is a proportionality constant, as well as α denotes the absorption coeffi-

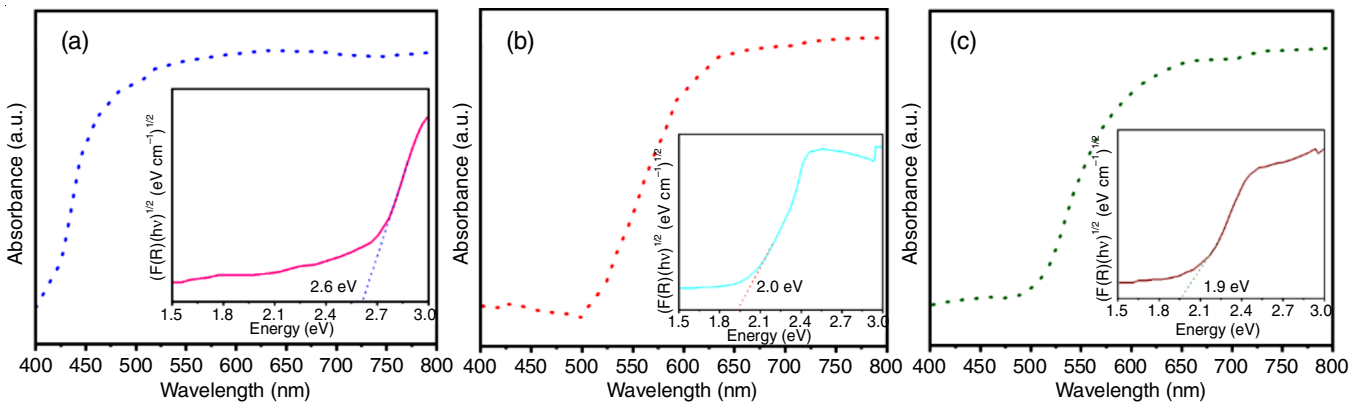

Fig. 3. The UV-Vis DRS spectra of (a) g-C_3N_4, (b) CdS, (c) g-C_3N_4/CdS. Tauc plots are shown in the inset

cient. By plotting $(\alpha h\nu)^2$ or $[F(R)h\nu]^2$ or $(h\nu)$, the bandgap energy can be determined by extending the linear portion for the graph in intersect the energy axis. This approach is commonly employed for estimating the optical bandgap of semiconductor materials.

Electrical conductivity: The charge transfer characteristics for the prepared samples were examined using electrochemical impedance spectroscopy (EIS), with the corresponding Nyquist plots. The diameter of the semicircle in these plots corresponds to the charge transfer resistance in the interface between the electrode as well as electrolyte [18]. A smaller semicircle indicates lower resistance, which reflects more efficient charge separation and transport. Among the samples tested, pristine *g*-C_3N_4 displayed the largest semicircle, indicating the highest charge transfer resistance and poorer conductivity [19]. CdS exhibited a comparatively smaller semicircle, suggesting better charge transport properties than *g*-C_3N_4. Significantly, the *g*-C_3N_4/CdS nanocomposite has been showed the smallest semicircle, revealing a significant reduced R_{ct} and enhanced interfacial charge transfer ability (Fig. 4).

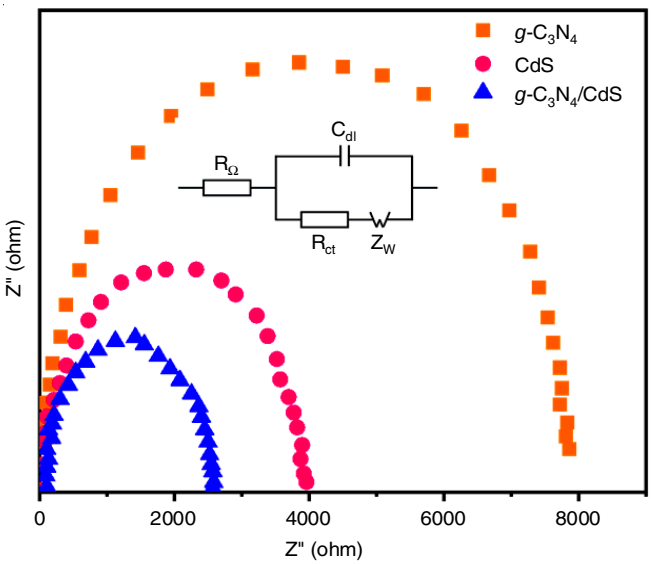

Fig. 4. Electron impedance spectroscopy of *g*-C_3N_4, CdS and *g*-C_3N_4/CdS along within visible light exposure, kλ ~ 420 nm

This improved conductivity in the *g*-C_3N_4/CdS composite was attributed in the synergistic interaction between *g*-C_3N_4 also CdS, which facilitates more enhance separation and movement for photogenerated charge carriers [21]. These enhanced charge transfer dynamics also imply reduced recombination for electron-hole pairs, contributing to the superior photocatalytic performance observed to the composite. Further confirming the improved interfacial charge kinetics within the *g*-C_3N_4/CdS heterostructure. Overall, these findings demonstrate that the composite formation plays a crucial role in enhancing photoelectrochemical properties, establishing *g*-C_3N_4/CdS as a promising candidate of visible-light-driven photocatalytic applications [29].

Photocatalytic activity: The photocatalytic activity for the *g*-C_3N_4/CdS nanocomposite has been evaluated by testing it abilities to degrading an organic pollutant, specifically AMX, under both dark as well as visible light conditions, following the outlined experimental procedure. The photocatalytic performance of the individual materials, *g*-C_3N_4 and CdS, as well as the *g*-C_3N_4/CdS nanocomposite, was assessed through the degradation for AMX within aqueous solution underneath visible light irradiation [30]. The decrease in the UV absorption peak intensity for AMX at 341 nm has used of monitor the degradation over irradiation time. The comparative degradation efficiencies of *g*-C_3N_4, CdS, also the *g*-C_3N_4/CdS nanocomposite are presented to Fig. 5a-c. Among them, the nanocomposite has been showed the highest degradation efficacy of 87.08% at 150 min of visible light exposure, with a rate constant (k) of 0.0149 min^{-1}. The rate constants of each catalyst were also determined (Fig. 6a), during the corresponding degradation efficacies (%) have shown in Fig. 6b [31]. Additionally, the pseudo-first-order kinetic analysis for AMX photodegradation is depicted in Fig. 6c [11]. These results demonstrate that the *g*-C_3N_4/CdS nanocomposite possesses a superior rate constant compared of the bare nanocomponents. The enhanced photocatalytic performance of the nanocomposite was attributed to the enhance separation as well as transfer for photo-induced electron-hole (e^-/h^+) pairs on the catalyst surface, it promotes greater photocatalytic activity [32].

The degradation rate efficiency (%) of AMX was calculated by using eqn. 4:

$$\text{Degradation rate, } \eta\ (\%) = \frac{C_{t=0} - C_t}{C_t} \times 100 \qquad (4)$$

where C_t denotes the concentration of AMX in specific intervals of time (t) and $C_{t=0}$ is the initial concentration of AMX.

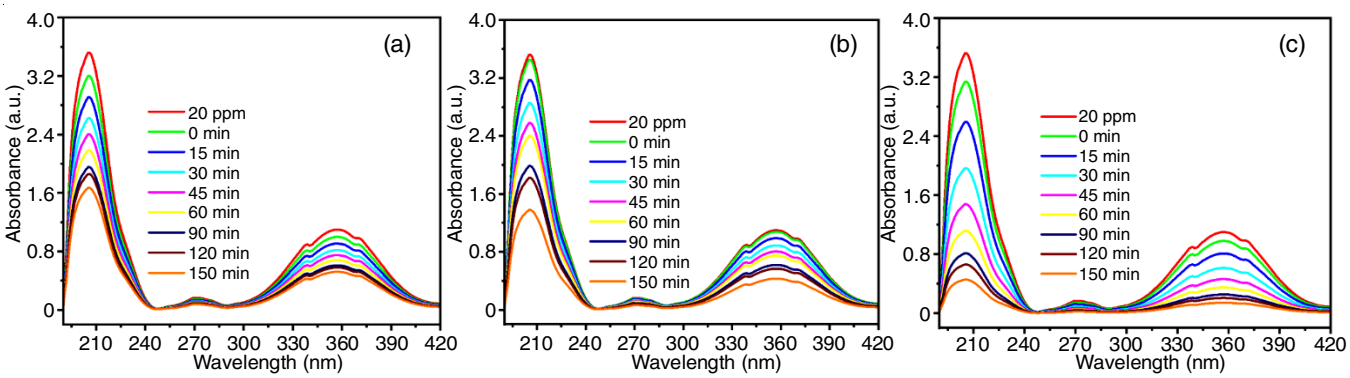

Fig. 5. The photocatalytic degradation of amoxicillin (AMX) using *g*-C_3N_4, CdS and *g*-C_3N_4/CdS nanocomposites

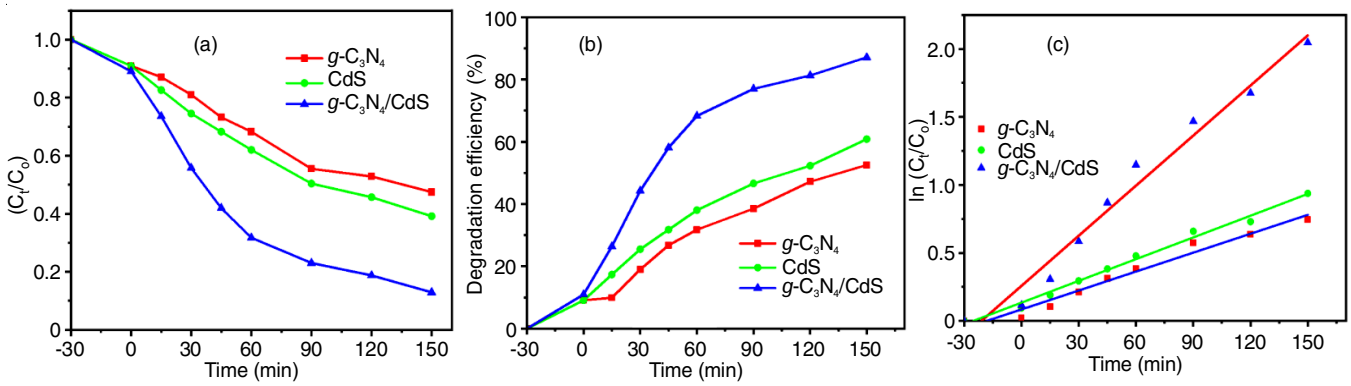

Fig. 6. The photodegradation rate (a), degradation efficacy (b), and pseudo-first-order kinetic plots (c) using g-C_3N_4, CdS and g-C_3N_4/CdS nanocomposites

Furthermore, the dynamic characteristics of the reaction was examined using a pseudo-first-order kinetic model, as described using eqn. 5 [33].

$$\ln\frac{C_o}{C_t} = kt \tag{5}$$

where C_o (mg/L), C_t (mg/L) are the initial as well as remaining AMX concentrations with the reaction processes; k is the apparent rate constant and t (min^{-1}) is the reaction time.

Proposed mechanism for the enhanced photocatalytic performance: In typical photocatalytic systems, hydroxyl radicals (•OH), superoxide radicals ($•O_2^-$), as well as photogenerated holes (h^+) act as key oxidizing agents [34]. To determine their specific roles, selective scavengers were used: isopropanol (IPA) of •OH, benzoquinone (BQ) for $•O_2^-$, as well as EDTA for h^+. The addition of EDTA led to only a slight reduction in AMX degradation, indicating a less significant role for photogenerated holes. Similarly, BQ caused a minor inhibitory effect, suggesting superoxide radicals contribute moderately [35].

However, tests with methanol caused a significant decrease in photocatalytic activity, revealing that photogenerated holes are indeed significant within the degradation processes. Based in these observations, a mechanism is proposed for the enhanced photocatalytic activities of the g-C_3N_4/CdS system. Upon visible light exposure, both g-C_3N_4 as well as CdS are excited due to their compatible band gap energies [3]. Electrons generated in g-C_3N_4 transfer efficiently of the conduction band for CdS through the close interfacial contact, while holes from CdS migrate in the valence band for g-C_3N_4. This charge transfer mechanism promotes effective separation for electron-hole pairs, extending their lifetime [20].

The accumulated holes in the valence band of g-C_3N_4 possess strong oxidative power, directly oxidizing AMX and simultaneously protecting CdS from photocorrosion. Meanwhile, electrons on CdS participate in reduction reactions such as proton reduction to hydrogen and converting adsorbed oxygen into superoxide radicals ($•O_2^-$), as well this can further produce hydroxyl radicals (•OH) [28]. The combined action of these reactive species, along with efficient charge separation enabled by g-C_3N_4/CdS heterojunction, drives the photocatalytic degradation for AMX efficiently. The enhanced photocatalytic performance for the g-C_3N_4/CdS composite arises from (i) improved the separation for charge carriers facilitated by the heterojunction as well as (ii) its high surface area and uniform photocatalyst dispersion, which boost light absorption and increase active sites [36].

The stability for the g-C_3N_4/CdS nanocomposite was evaluated through recyclability tests conducted over three consecutive cycles of AMX photodegradation (Fig. 7a) [25]. After each cycle, the photocatalyst was recovered by centrifugation, thoroughly rinsed within deionized water of remove any residual impurities and dried at 60 ºC before being reused [30]. As shown in Fig. 7a, the photocatalytic activities exhibited a gradual decrease over the cycles. During the initial cycle, about 87.08% of AMX was degraded after 150 min of visible light irradiation, which decreased to roughly 82.08% in the second cycle and further to approximately 77.08% in the third cycle [37]. Despite this slight reduction in efficiency, the nanocomposite maintained strong photocatalytic performance, demonstrating good durability and reusability over multiple uses.

Photocatalytic mechanism:

$$\frac{g\text{-}C_3N_4}{CdS} + h\nu \longrightarrow e^- + h^+ \tag{6}$$

$$e^- + O_2 \longrightarrow •O_2^- \tag{7}$$

$$2e^- + O_2 + 2H^+ \longrightarrow H_2O_2 \tag{8}$$

$$H_2O_2 + •O_2^- \longrightarrow •OH + OH^- + O_2 \tag{9}$$

$$h^+ + OH^- \longrightarrow •OH + H^+ \tag{10}$$

$$•OH + h^+ + AMX \longrightarrow \text{Degradation pollutants} \tag{11}$$

The enhanced degradation efficiency of AMX contaminants by the g-C_3N_4/CdS nanocomposite could be attributed of the synergistic combination of increased surface area as well as improved visible-light absorption.

Scheme-II presents the proposed mechanism underlying the superior photocatalytic degradation for organic pollutants like AMX facilitated through this nanocomposite. Understanding the band edge positions is essential for assessing the photocatalytic performance, as adjustments to these band edge values significantly impact the overall effectiveness of catalyst.

$$E_{VB} = X - E^e + 0.5 \times E_g \tag{12}$$

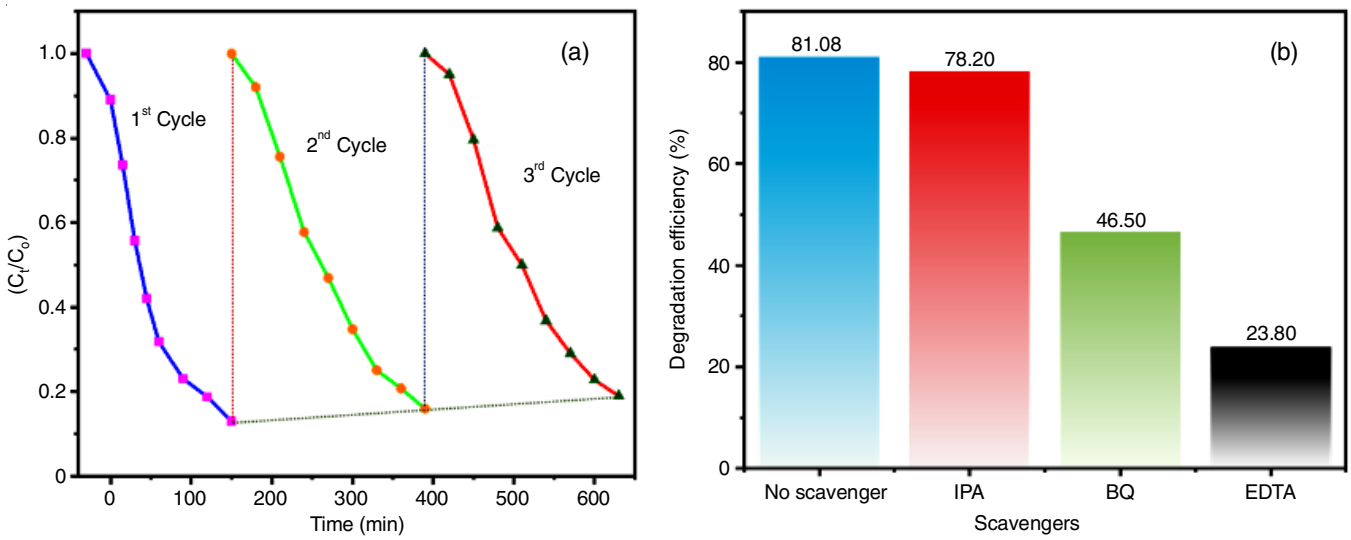

Fig. 7. (a) The reusability data of g-C_3N_4/CdS photocatalytic nanocomposite and (b) the effect of various reactive species scavengers on the photocatalytic degradation efficacy of amoxicillin (AMX)

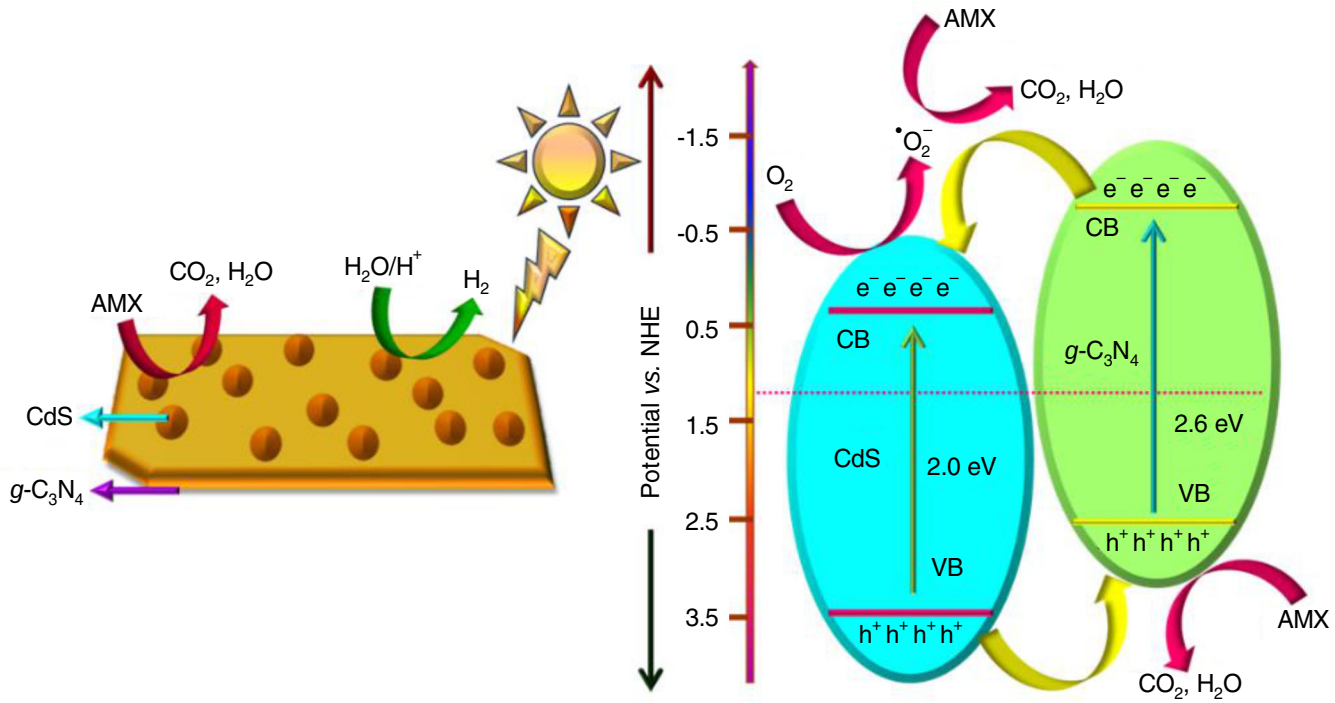

Scheme-II: Mechanism of amoxicillin (AMX) degradation using g-C_3N_4/CdS nanocomposite

$$E_{CB} = E_{VB} - E_g \quad (13)$$

The mechanism proposed in **Scheme-II** emphasizes the importance of the valence band edge potential (E_{VB}) as well as conduction band edge potential (E_{CB}) at determining the photocatalytic efficiency of the system. A crucial factor in this context is the electronegativity (X) for the materials. For g-C_3N_4 and CdS, the electronegativity values were 6.16 eV also 4.73 eV, accordingly [38]. The electron energy (E_e) is taken as approximately 4.5 eV under standard conditions, while the band gap energies (E_g) are 2.6 eV for g-C_3N_4 and 2.0 eV of CdS. These parameters are essential for calculating the conduction and valence band edge potentials (eqns. 12 and 13). Specifically, the E_{CB} and E_{VB} for g-C_3N_4 were –1.11 eV as well as +1.39 eV, correspondingly, while for CdS, the E_{CB} is –0.32 eV, all relative of the normal hydrogen electrode (NHE) [29]. These values offer important insights into the underlying mechanisms driving the photodegradation for pollutants like AMX under light exposure using the g-C_3N_4/CdS nanocomposite [25].

Furthermore, the oxidation for electron (hole) h^+ as well water molecules occur *via* the valence bands of CdS and g-C_3N_4, generating reactive h^+. The standard potentials for these reactions are E^o–$OH/OH^{\bullet-}$ = +3.01 eV and E^o–$OH/OH^{\bullet}$ = +3.66 eV, accordingly. Importantly, electrons from the conduction band for CdS transfer energetically in the valence band for g-C_3N_4, creating an S-scheme heterojunction between the two

materials. In this heterojunction, CdS acts as an efficient redox mediator, facilitating electron transfer between g-C_3N_4 and CdS [33]. This S-scheme configuration promotes enhance separation for photo-induced electron-hole pairs, extending their lifetime also thus enhancing the overall photocatalytic activity of the system. As a result, the g-C_3N_4/CdS nanocomposite exhibits superior photocatalytic performance due to efficient charge separation, strong absorption for visible light, potential magnetic effects, also its capability of degrade organic contaminates to wastewater effectively [9].

Furthermore, the photoexcited electrons on g-C_3N_4 can reduce adsorbed oxygen molecules to form superoxide radicals ($O_2^{\bullet-}$). These reactive species play a key role at breaking down AMX contaminants and can also promote the formation of H_2O_2 [3], as detailed in eqns. 6-11. Concurrently, underneath visible light, the photogenerated holes (h^+) on CdS may transfer to the valence band for g-C_3N_4, where they oxidize water molecules, producing hydroxyl radicals ($OH^{\bullet}$) [39,40]. These radicals were strong oxidizers that further contribute to the degradation for organic contaminates. The generated superoxide radicals react within AMX molecules, leading to their decomposition into harmless substances such as H_2O and CO_2 [41]. This degradation pathway underscores the high efficiency for the g-C_3N_4/CdS nanocomposite at treating organic contaminants, highlighting its promising potential of environmental cleanup applications.

Conclusion

In this study, a g-C_3N_4/CdS binary nanocomposite within visible-light activity has been successfully prepared utilizing the wet impregnation technique as well as assessed of its ability to degrade the antibiotic amoxicillin (AMX). The characterization through XRD, SEM, UV-DRS, also EIS confirmed the structural as well optical properties of nanocomposite. The photocatalyst achieved a high AMX degradation efficiency of 87.08% within a rate constant (k) with 0.0149 min^{-1}, following an S-scheme charge transfer mechanism. This improved photocatalytic performance is linked of its narrowed band gap of 1.9 eV as well as more enhance separation of photogenerated charge carriers compared to bare g-C_3N_4, CdS, also their physical mixture. Reactive species trapping experiments revealed that photogenerated holes (h^+) as well as hydroxyl radicals ($^{\bullet}OH$), superoxide radicals ($O_2^{\bullet-}$), play major roles in the degradation process. The catalyst also showed good stability, maintaining 77.08% of its photocatalytic activity after three reuse cycles. These findings highlight the g-C_3N_4/CdS nanocomposite as a highly enhance, stable and reusable photocatalyst with strong potential of environmental cleanup. This study contributes valuable knowledge toward the design for effective visible-light-driven photocatalysts of removing emerging organic pollutants from water systems.

ACKNOWLEDGEMENTS

The authors express their sincere gratitude to Saveetha Institute of Medical and Technical Sciences, Saveetha University, Chennai, India, for their generous support in facilitating this research work.

CONFLICT OF INTEREST

The authors declare that there is no conflict of interests regarding the publication of this article.

REFERENCES

1. K.D. Radosavljevic, A.V. Golubovic, M.M. Radišic, A.R. Mladenovic, D.Z. Mijin and S.D. Petrovic, *Chem. Ind. Chem. Eng. Q.*, **23**, 187 (2017); https://doi.org/10.2298/CICEQ160122030R
2. H.F. Rocha, V. Silva, D.L. Lima and V. Calisto, *Case Stud. Chem. Environ. Eng.*, **9**, 100724 (2024); https://doi.org/10.1016/j.cscee.2024.100724
3. I.F. Silva, I.F. Teixeira, R.D. Rios, G.M. do Nascimento, I. Binatti, H.F. Victória, K. Krambrock, L.A. Cury, A.P.C. Teixeira and H.O. Stumpf, *J. Hazard. Mater.*, **401**, 123713 (2021); https://doi.org/10.1016/j.jhazmat.2020.123713
4. A.S. Oberoi, Y. Jia, H. Zhang, S.K. Khanal and H. Lu, *Environ. Sci. Technol.*, **53**, 7234 (2019); https://doi.org/10.1021/acs.est.9b01131
5. R.K. Langbehn, C. Michels and H.M. Soares, *Environ. Pollut.*, **275**, 116603 (2021); https://doi.org/10.1016/j.envpol.2021.116603
6. P. Darvishi, S.A. Mousavi, A. Mahmoudi and D. Nayeri, *Environ. Sci.: Water Res. Technol.*, **9**, 11 (2023); https://doi.org/10.1039/D1EW00912E
7. I.Y. Qudsieh, M.A. Ali and I.M. Maafa, *Crystals*, **15**, 167 (2025); https://doi.org/10.3390/cryst15020167
8. H. Xu, W.J. Cooper, J. Jung and W. Song, *Water Res.*, **45**, 632 (2011); https://doi.org/10.1016/j.watres.2010.08.024
9. M. Saeed, M. Muneer, A.U. Haq and N. Akram, *Environ. Sci. Pollut. Res. Int.*, **29**, 293 (2022); https://doi.org/10.1007/s11356-021-16389-7
10. F.B. Li and X.Z. Li, *Chemosphere*, **48**, 1103 (2002); https://doi.org/10.1016/S0045-6535(02)00201-1
11. R. Ghamarpoor, A. Fallah and M. Jamshidi, *ACS Omega*, **9**, 25457 (2024); https://doi.org/10.1021/acsomega.3c08717
12. S.C. Yan, Z.S. Li and Z.G. Zou, *Langmuir*, **25**, 10397 (2009); https://doi.org/10.1021/la900923z
13. M. Hamity, R.H. Lema, C.A. Suchetti and H.E. Gsponer, *J. Photochem. Photobiol. Chem.*, **200**, 445 (2008); https://doi.org/10.1016/j.jphotochem.2008.09.010
14. F. Soleimani and A. Nezamzadeh-Ejhieh, *J. Mater. Res. Technol.*, **9**, 16237 (2020); https://doi.org/10.1016/j.jmrt.2020.11.091
15. Z. Yu, B. Yin, F. Qu and X. Wu, *Chem. Eng. J.*, **258**, 203 (2014); https://doi.org/10.1016/j.cej.2014.07.041
16. Y. Song, J. Tian, S. Gao, P. Shao, J. Qi and F. Cui, *Appl. Catal. B*, **210**, 88 (2017); https://doi.org/10.1016/j.apcatb.2017.03.059
17. S.C. Yan, Z.S. Li and Z.G. Zou, *Langmuir*, **26**, 3894 (2010); https://doi.org/10.1021/la904023j
18. N. Pourshirband, A. Nezamzadeh-Ejhieh and S.N. Mirsattari, *Spectrochim. Acta A Mol. Biomol. Spectrosc.*, **248**, 119110 (2021); https://doi.org/10.1016/j.saa.2020.119110
19. B. Shao, X. Liu, Z. Liu, G. Zeng, W. Zhang, Q. Liang, Y. Liu, Q. He, X. Yuan, D. Wang, S. Luo and S. Gong, *Chem. Eng. J.*, **374**, 479 (2019); https://doi.org/10.1016/j.cej.2019.05.202
20. S. Shenoy, K. Tarafder and K. Sridharan, *Physica B*, **595**, 412367 (2020); https://doi.org/10.1016/j.physb.2020.412367
21. J. Fang, K. Xie, Q. Kang and Y. Gou, *J. Sci. Adv. Mater. Dev.*, **7**, 100409 (2022); https://doi.org/10.1016/j.jsamd.2021.100409
22. S. Al Mamari, F.E. Suliman, Y. Kim and R. Selvaraj, *Adv. Powder Technol.*, **34**, 104026 (2023); https://doi.org/10.1016/j.apt.2023.104026
23. G. Liu, M. Liao, Z. Zhang, H. Wang, D. Chen and Y. Feng, *Sep. Purif. Technol.*, **244**, 116618 (2020); https://doi.org/10.1016/j.seppur.2020.116618

24. X. Sun, K. He, Z. Chen, H. Yuan, F. Guo and W. Shi, *Sep. Purif. Technol.*, **324**, 124600 (2023); https://doi.org/10.1016/j.seppur.2023.124600
25. K. Li, M. Chen, L. Chen, S. Zhao, W. Xue, Z. Han and Y. Han, *Processes*, **11**, 528 (2023); https://doi.org/10.3390/pr11020528
26. S.S.A. Al-Razzaq and A.J. Ghazai, *AIP Conf. Proc.*, **3303**, 030002 (2025); https://doi.org/10.1063/5.0266765
27. J.H. Pereira, A.C. Reis, V. Homem, J.A. Silva, A. Alves, M.T. Borges, R.A.R. Boaventura, V.J.P. Vilar and O.C. Nunes, *Water Res.*, **65**, 307 (2014); https://doi.org/10.1016/j.watres.2014.07.037
28. D. Dimitrakopoulou, I. Rethemiotaki, N.P. Xekoukoulotakis, D. Venieri, Z. Frontistis and D. Mantzavinos, *J. Environ. Manage.*, **98**, 168 (2012); https://doi.org/10.1016/j.jenvman.2012.01.010
29. M. Qutob, F. Shakeel, P. Alam, S. Alshehri, M.M. Ghoneim and M. Rafatullah, *Environ. Res.*, **214**, 113833 (2022); https://doi.org/10.1016/j.envres.2022.113833
30. J. Wang, G. Wang, B. Cheng, J. Yu and J. Fan, *Chin. J. Catal.*, **42**, 56 (2021); https://doi.org/10.1016/S1872-2067(20)63634-8
31. M. Caux, F. Fina, J.T. Irvine, H. Idriss and R. Howe, *Catal. Today*, **287**, 182 (2017); https://doi.org/10.1016/j.cattod.2016.11.007
32. K. Hemkumar, P. Ananthi and A. Pius, *J. Mol. Liq.*, **425**, 127274 (2025); https://doi.org/10.1016/j.molliq.2025.127274
33. S. Rani, A. Garg and N. Singh, *Toxicol. Environ. Chem.*, **103**, 137 (2021); https://doi.org/10.1080/02772248.2021.1931214
34. J. Wang, J. Feng and C. Wei, *Appl. Surf. Sci.*, **609**, 155324 (2023); https://doi.org/10.1016/j.apsusc.2022.155324
35. N. Maldonado-Carmona, G. Piccirillo, J. Godard, K. Heuzé, E. Genin, N. Villandier, M.J.F. Calvete and S. Leroy-Lhez, *Photochem. Photobiol. Sci.*, **23**, 587 (2024); https://doi.org/10.1007/s43630-024-00536-3
36. H.T.A. Alamir, R.R. Abass, O.H. Salah, M.M. Karim, S. Ahjel, S.J. Al-Shuwaili, W.D. Kadhim and R.A. Ahmed, *Adv. J. Chem.*, **7A**, 438 (2024); https://doi.org/10.48309/ajca.2024.449003.1501
37. Q. Li, H. Kong, P. Li, J. Shao and Y. He, *J. Hazard. Mater.*, **373**, 437 (2019); https://doi.org/10.1016/j.jhazmat.2019.03.066
38. M. Chaudhuri, M.Z.B.A. Wahap and A.C. Affam, *Desalination Water Treat.*, **51**, 7255 (2013); https://doi.org/10.1080/19443994.2013.773565
39. B.S. Silva and A.L. de Castro Peixoto, *Braz. J. Chem. Eng.*, **41**, 149 (2024); https://doi.org/10.1007/s43153-023-00364-5
40. D. Balarak, N. Mengelizadeh, P. Rajiv and K. Chandrika, *Environ. Sci. Pollut. Res. Int.*, **28**, 49743 (2021); https://doi.org/10.1007/s11356-021-13525-1
41. T.T. Nguyen, S.N. Nam, J. Son and J. Oh, *Sci. Rep.*, **9**, 9349 (2019); https://doi.org/10.1038/s41598-019-45644-8